LETTERS
PUBLISHED ONLINE: 9 MARCH 2014 | DOI: 10.1038/NCLIMATE2144
nature climate change

Distinct effects of anthropogenic aerosols on tropical cyclones

Yuan Wang[1,2*], Keun-Hee Lee[1,3], Yun Lin[1], Misti Levy[1] and Renyi Zhang[1,4*]

Long-term observations have revealed large amplitude fluctuations in the frequency and intensity of tropical cyclones (TCs; refs 1–4), but the anthropogenic impacts, including greenhouse gases and particulate matter pollution[4,5], remain to be elucidated. Here, we show distinct aerosol effects on the development of TCs: the coupled microphysical and radiative effects of anthropogenic aerosols result in delayed development, weakened intensity and early dissipation, but an enlarged rainband and increased precipitation under polluted conditions. Our results imply that anthropogenic aerosols probably exhibit an opposite effect to that of greenhouse gases, highlighting the necessity of incorporating a realistic microphysical–radiative interaction of aerosols for accurate forecasting and climatic prediction of TCs in atmospheric models.

Tropical cyclones (TCs) represent one of the most destructive natural weather phenomena, with an annual global occurrence of about 90 events[2]. As a large and complex convective system associated with enormous surface enthalpy fluxes, the frequency and intensity of TCs are regulated by several environmental conditions, including sea surface temperature (SST), vertical wind shear, vorticity, and humidity of the free troposphere[6]. Both observational and modelling studies have assessed changes in the frequency and intensity of TCs in a warming world, but the results often conflict because of limitations in the global historical records and uncertainties in global climate models. For example, although regional and global data analyses indicate a trend of more frequent and intense TCs during recent decades[1,2], explicit and downscaled simulations using global climate models often project decreases in the globally averaged TC frequency because of greenhouse gas warming[4]. At present, the detection of long-term TC trends and their attribution to the rising level of greenhouse gases remain uncertain[4].

In addition, atmospheric aerosols may also impact oceanic cyclones by modifying thermodynamic and microphysical conditions[5,7–11]. The warming effect due to accumulating greenhouse gases along with the cooling effect exerted by anthropogenic aerosols has been linked to long-term trends in tropical Atlantic warmth and increasingly stronger hurricanes in recent decades[12]. Satellite analysis suggests that cooling over the tropical North Atlantic by elevated aerosols suppressed TC activities in the western Atlantic and the Caribbean during the 2006 hurricane season[13]. Recent studies of mineral dust reveal a large influence from the Sahara Desert on the formation and development of Atlantic hurricanes by modulating the cloud hydrometeor contents, diabatic heating distribution, and thermodynamic structure[14,15].

The microphysical role of aerosols acting as cloud condensation nuclei (CCN) and altering TCs has been examined in several numerical studies. Cloud-resolving model simulations indicate that invigorated convection contributes to increased lightning activity at the periphery of TCs, but weakened convection and intensity in the eyewall region[16–18]. Moreover, the plausible impact of submicron CCN seeding may suppress warm rain and weaken TCs as a result of lower-level evaporative cooling of unprecipitated raindrops[19]. However, few studies have examined the coupled microphysical and radiative effects of aerosols by considering the microphysical–radiative-dynamic interaction for TCs, even though aerosol-induced cooling of SST and the consequent feedback on the cyclogenesis in the ocean–atmosphere system have been suggested[7,13].

In this study we quantify and isolate the microphysical and radiative effects of anthropogenic aerosols on TCs. Direct and semi-direct aerosol radiative forcings are evaluated by means of a radiative module interacting with explicit cloud microphysics[20,21]. Three aerosol scenarios are simulated in our numerical experiments (Methods and Supplementary Fig. 1), representing a clean maritime case (C-case), a polluted case (P-case), and a polluted case with the aerosol radiative forcing (PR-case) from light absorbing aerosols. The aerosol number concentrations in the P-case and PR-case are identical and are five times higher than that in the C-case, and the PR-case contains 5% of black carbon internally mixed with ammonium sulphate. Those aerosol properties are consistent with atmospheric field measurements throughout the Gulf of Mexico region[22,23] and satellite observations of maritime conditions under the influence of continental pollution[9,10].

The TC intensity is commonly represented by the maximum surface wind speed and minimum surface pressure. Although all simulations reproduce the typical features of the TC evolution (Fig. 1), namely an intensification stage (<48 h) and a dissipation stage (>48 h), the simulated TC exhibits distinct development patterns under the different aerosol scenarios (Supplementary Figs 2–4). For example, upon reaching the maximal intensity at 48 h, the peak maximum surface wind speed is lower whereas the nadir minimum surface pressure is higher under the two polluted cases, both indicating a weakened TC. Also, the simulated TC in the two polluted cases exhibits noticeably delayed intensification, as evident in the slower increase (decrease) in the maximum surface wind speed (minimum surface pressure). The occurrences of the peak maximum surface wind speed and the nadir minimum surface pressure are delayed by about 10 h in the two polluted cases. The maximum surface wind speed and minimum surface pressure are comparable between the P-case and PR-case, except that the

[1]Department of Atmospheric Sciences, Texas A&M University, Center for Atmospheric Chemistry and the Environment, College Station, Texas 77843-3150, USA, [2]Jet Propulsion Laboratory, California Institute of Technology, Pasadena, California 91109, USA, [3]Korean Meteorological Administration, Seoul 156-720, South Korea. [4]State Key Joint Laboratory of Environmental Simulation and Pollution Control, College of Environmental Sciences and Engineering, Peking University, Beijing 100871, China. *e-mail: Yuan.Wang@jpl.nasa.gov; renyi-zhang@geos.tamu.edu

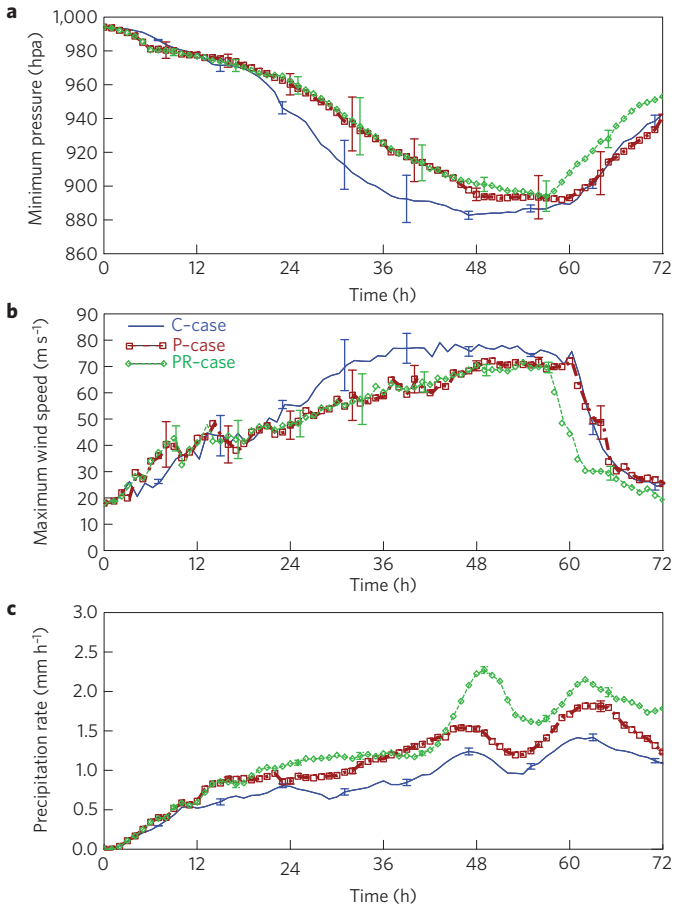

Figure 1 | Tropical cyclone temporal evolution. Minimum surface pressure (**a**), maximum wind speed (**b**) and precipitation rate (**c**) for the three different aerosol scenarios: a clean maritime case (C-case) in blue, a polluted case (P-case) in dark red and a polluted case with aerosol radiative forcing (PR-case) in green. Error bars (one s.d.) are estimated from five ensemble simulations with different initial random temperature perturbations.

PR-case shows earlier dissipation. On the other hand, the domain average amount of precipitation is much larger in the two polluted cases than that in the clean maritime case. The largest difference in precipitation between the clean and polluted cases occurs after the TC reaches its peak intensity at 48 h. A comparison between the P-case and PR-case indicates that the aerosol radiative effect contributes to further enhanced precipitation.

Recent studies have indicated that deep convection systems such as TCs are highly sensitive to initial perturbations of the meteorological parameters[24–26]. To evaluate the sensitivity of our simulations to initial meteorological perturbations, five ensemble-member runs with different initial random temperature perturbations were carried out for each aerosol condition (the C-, P- or PR-case). The potential errors in the predicted maximum wind speed, minimum surface pressure and precipitation are within 3%, 25% and 5%, respectively, verifying the robustness of the simulated aerosol effects. A further twenty simulations were performed with identical initial and boundary meteorological conditions, but with a varying initial aerosol number concentration from 100 to 2,000 cm^{-3} at the surface (Supplementary Figs 2 and 3). The response of the TC evolution to increasing aerosols is almost monotonic, showing a consistently decreasing maximum surface wind speed, increasing minimum surface pressure, and increasing amount of precipitation as the aerosol concentration is successively increased from the pristine (<500 cm^{-3}) to polluted (>1,000 cm^{-3}) conditions.

Figure 2 depicts simulated radar reflectivities for the three aerosol scenarios. In the C-case, precipitation occurs mainly in the eyewall region, as evident from the maximum radar reflectivity, which is located within a distance of 50 km from the TC centre. For the P-case, the precipitation is reduced in the eyewall region, but is significantly enhanced in the rainband beyond a distance of 100 km from the TC centre. An increasing amount of CCN yields larger amounts of liquid and ice clouds in the rainband region, because of an increased cloud droplet number concentration, suppressed warm precipitation, and enhanced mixed-phase processes. Hence, the microphysical effect of aerosols leads to an invigorated convection and enhanced precipitation in the rainband because of a greater release of latent heat (Supplementary Fig. 5). On the other hand, an invigorated rainband region hinders the transport of sensible and latent enthalpies toward the TC centre, because the inflow of warm, moist air in the planetary boundary layer to maintain the TC development is blocked by the active rainband and is substituted by colder, drier air generated from the downdraft of the rainband region. The radiative effect of light-absorbing aerosols causes warming in the lower troposphere, which further strengthens the lower-level convection and enhances precipitation in the rainband region, leading to a further enhanced radar reflectivity in the rainband beyond a distance of 150 km from the TC centre in the PR-case. Similar to the microphysical effect, the radiative effect of light-absorbing aerosols also inhibits transport of sensible enthalpy and moisture by the inflow and further reduces precipitation in the eyewall region during the dissipation stage.

The invigorated rainband and weakened eyewall under elevated aerosol conditions are also revealed by examining the air equivalent potential temperature (θ_e) in the bottom level of the troposphere (Fig. 3), which illustrates the thermodynamic instability of the TC system[27]. The P-case (Fig. 3b) exhibits a distinctively decreased θ_e both in the eyewall and rainband regions compared to the C-case (Fig. 3a). This is explained by invigorated convection in the rainband, which effectively consumes θ_e in the P-case. Furthermore, the enhanced downdraft originating from falling hydrometeors and their subsequent melting and evaporative cooling results in drier, colder air in the planetary boundary layer, leading to further suppression of θ_e. The reduced θ_e near the eyewall region in the P-case indicates that the instability in the TC centre is reduced because colder, drier air is advected into the eyewall region. A comparison of θ_e between the P-case and PR-case (Fig. 3b,c) shows that θ_e is enhanced both in the eyewall and rainband regions at 48 h, probably as a result of heating due to light-absorbing aerosols in the lower troposphere. As advection of aerosols from the model lateral boundaries occurs at the near-surface level, heating caused by light-absorbing aerosols near the surface in the PR-case destabilizes the atmosphere at the TC periphery and enhances convection in the rainband region when the TC reaches its peak intensity. The combined aerosol microphysical and radiative effects lead to significantly enhanced precipitation in the rainband, which is responsible for the smallest θ_e at 60 h in the PR-case, whereas the coldest, driest inflow during the dissipation stage of the PR-case accounts for the weakest intensity and earliest dissipation of the simulated TC.

Our results provide a quantitative assessment of the microphysical and radiative effects of anthropogenic aerosols on the development of TCs. As depicted in Fig. 4, by serving as CCN, aerosols increase the number of cloud droplets and the release of latent heat, invigorating the peripheral rainband. Light-absorbing aerosols heat the lower troposphere and further enhance the convection in the rainband. The combined aerosol effects increase rainband precipitation (Supplementary Fig. 6), but suppress eyewall development by reducing enthalpy and moist transport of the

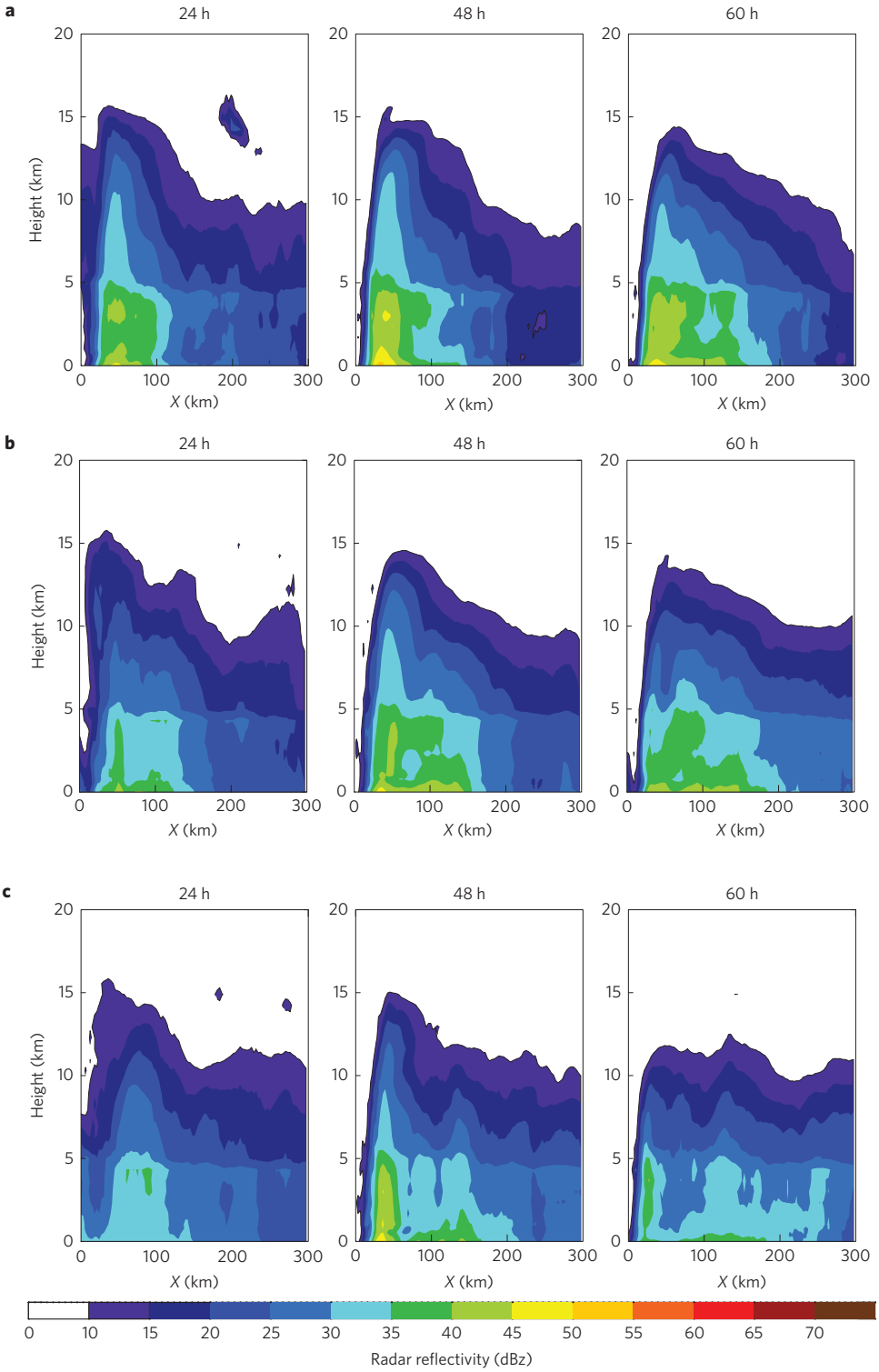

Figure 2 | Vertical–radial cross-sections of azimuthally averaged radar reflectivity. Simulations for the three aerosol scenarios: C-case (**a**), P-case (**b**), and PR-case (**c**). The three time periods of 24, 48 and 60 h correspond to the intensification stage, the maximal intensity and the dissipation stage of the TC, respectively.

lower-level inflow. Overall, the coupled aerosol effects result in a noticeably delayed, weakened and early dissipated TC, but significantly enhanced precipitation in an enlarged rainband region. Hence, our results corroborate the proposed mechanism of aerosol-induced TC weakening from the previous modelling studies, which suggest that the microphysical effect of continental aerosols invigorates convection at the TC periphery but reduces the lower-level inflow[16–19,28]. On the other hand, we further demonstrate that the radiative effect of light-absorbing aerosols reinforces the microphysical effect, leading to an even weaker intensity but increased precipitation of TCs.

If the maximum surface wind speed (or the minimum surface pressure) is considered as the deterministic representation of the TC intensity, elevated anthropogenic aerosols may mask or

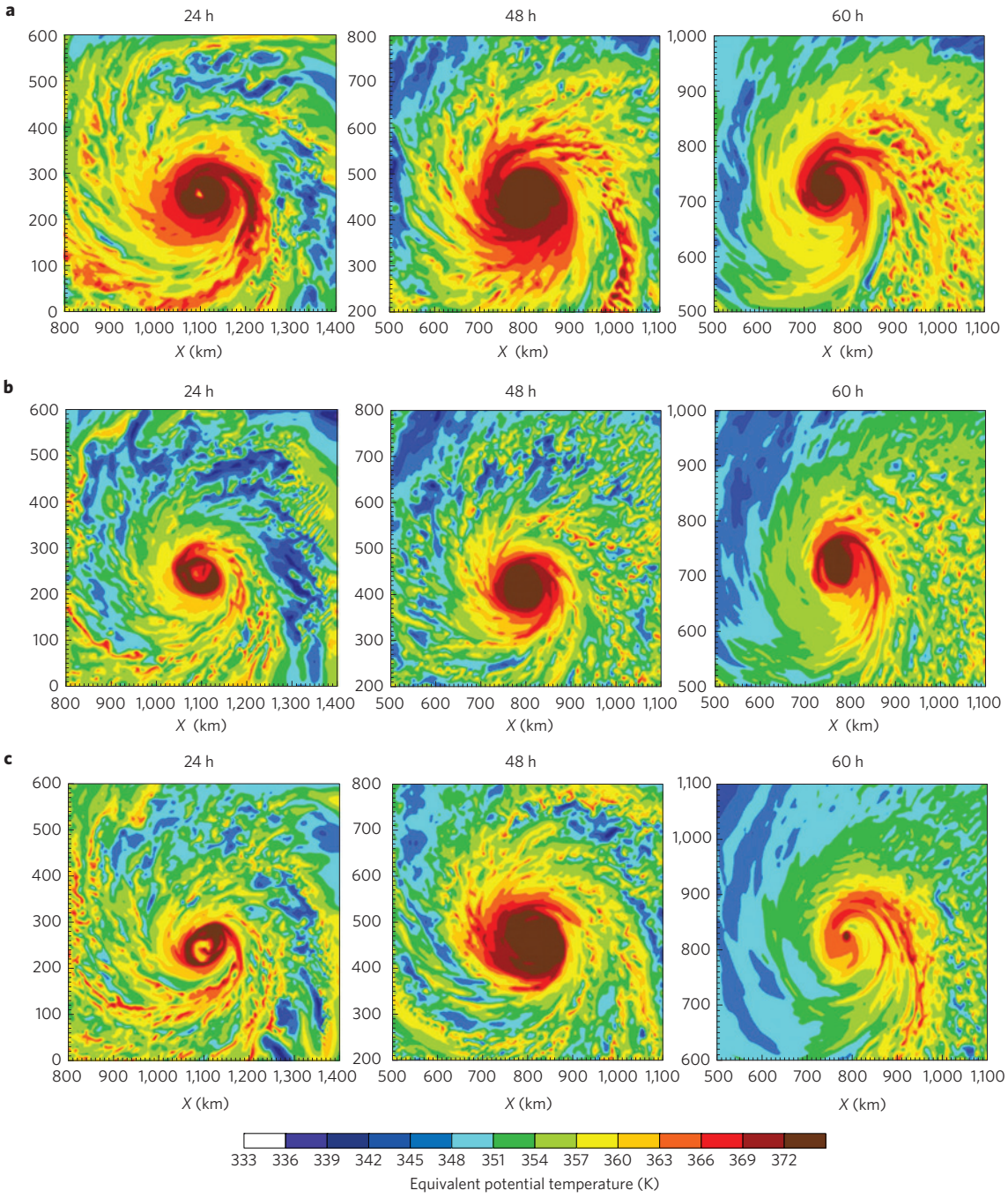

Figure 3 | Horizontal distribution of the equivalent potential temperature. Value of θ_e at the lowest model level in the three simulations: C-case (**a**), P-case (**b**) and PR-case (**c**).

even cancel out the effect of more intensive TCs caused by increasing greenhouse gases, as previously suggested on the basis of regional and global data analyses[1,2]. Hence, the anthropogenic influences of greenhouse gases and aerosols probably exhibit opposing behaviours on the development of TCs. This may be particularly true over the Pacific, which is under the influence of increasingly intense Asian anthropogenic pollution outflows[8,9] and biomass burning plumes from Southeast Asia[29]. Furthermore, it is essential that a comprehensive index to represent the potential destructiveness[1], including not only the wind speed but also precipitation, is developed when long-term measurements are employed to construct the historical inter-annual variation of TCs[1,30] and evaluate the effects of aerosols[5,7]. Because of the enormous economic and societal impacts, it is imperative that the microphysical and radiative effects of anthropogenic aerosols are fully considered in accurate forecasting and climatic projections of TCs in atmospheric mesoscale and global climate models.

Methods

A two-moment bulk microphysical scheme under the framework of the WRF model (Version 3.1.1), initially developed by Li *et al.*[20], is employed in this study to assess the effects of aerosols. The microphysical scheme calculates the time-dependent mass-mixing ratios and the number concentrations of five types of hydrometeors—cloud water, rain water, ice crystals, snow flakes, and graupels—along with the aerosol mass-mixing ratio, surface area and number concentration. To consider the radiative effect of aerosols, a module is incorporated into the Goddard Shortwave Radiation Scheme to interact with

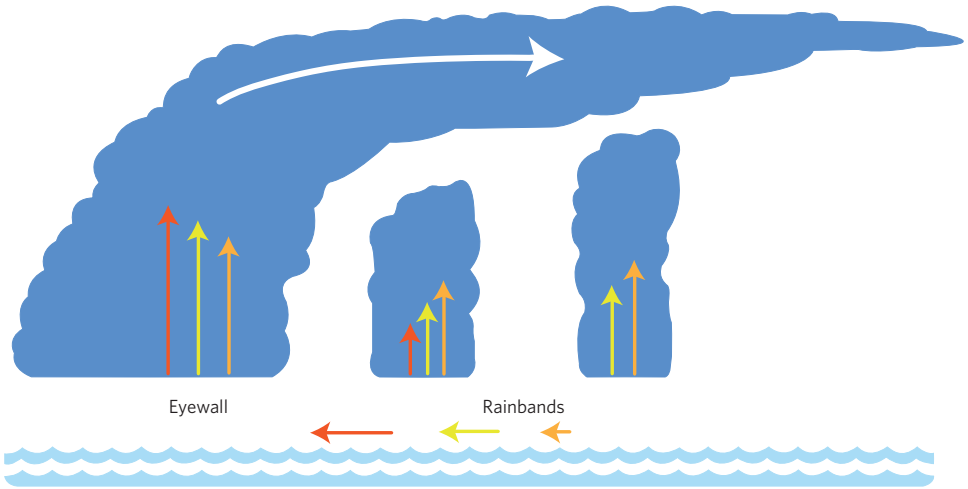

Figure 4 | Schematic of the microphysical and radiative effects of anthropogenic aerosols on TCs. The development of TCs is characterized by the vertical velocities in the peripheral rainband and eyewall regions (vertical arrows) and the lower-level inflow (horizontal arrows) that supplies enthalpy and moisture to the TC centre. The C-case (red) corresponds to the strongest inflow and convection in the eyewall region. For the P-case (yellow), the microphysical effect suppresses warm precipitation, but enhances mixed-phase processes, leading to invigorated rainband development. For the PR-case (orange), convective development in the rainband region is further enhanced because of lower-level heating by absorbing aerosols. The strongest convective development in the rainbands (the longest vertical orange arrow in the outer rainband) because of the coupled aerosol microphysical and radiative effects leads to the weakest inflow (the shortest horizontal orange arrow) and eyewall development (the shortest orange arrow among the three vertical lines in the eyewall region).

aerosol and cloud microphysics and calculate online the wavelength-dependent aerosol optical properties, including aerosol optical depth, asymmetry factor and single scattering albedo (SSA; ref. 21).

We perform numerical simulations relevant to the conditions of Hurricane 'Katrina' from 00:00 UTC 27 August 2005 to 00:00 UTC 30 August 2005 using a two-way nested grid of the WRF model. A 9-km outer domain with a nest on a 3-km mesh is integrated (see Supplementary Fig. 1a). Simulations are initialized from six-hourly NCEP Final Operational Global Analysis (1°× 1°) and use the NCEP global SST data. In our current cloud-resolving WRF model, no convective parametrization is employed in the two-mesh domain.

In this study, clean maritime and polluted continental aerosols are assumed to consist of both seasalt (NaCl) and ammonium sulphate ($(NH_4)_2SO_4$). CCN activation is treated using the Khöler theory[20,31]. A seasalt production scheme is included to generate NaCl aerosols over the ocean surface[9,10]. For the initial and boundary concentrations at the surface level, the concentrations of $(NH_4)_2SO_4$ aerosols are 200 and 1000 cm^{-3}, respectively, under the clean maritime condition (C-case) and the polluted conditions (P-case and PR-case). All simulations are initialized using a vertical aerosol profile with the maximal number concentration at the surface and a decreasing concentration with altitude (Supplementary Fig. 1b). In the case of the aerosol radiative effect (PR-case), aerosols are assumed to contain an internal black carbon core surrounded by ammonium sulphate and the mass-mixing ratios are assumed to be 5 % for black carbon and 95 % for ammonium sulphate. The SSA of internally mixed black carbon and ammonium sulphate aerosols in this study is calculated to be about 0.9 at the mid-visible range throughout the simulations. Atmospheric field measurements[22,23] reveal that black carbon accounts for 5–10% of the aerosol content and the measured SSA ranges from 0.7 to 0.9 throughout the Gulf of Mexico region, including from shipboard (NOAA R/V *Ronald H. Brown*) measurements during the 2006 Gulf of Mexico Atmospheric Composition and Climate Study. The aerosol loading is about 7 μg m^{-3} from the field measurements, consistent with those in our P- and PR-cases. On the global scale, the mass fraction of black carbon in anthropogenic aerosols is about 4%, which is simulated in the global climate model[32] using the latest emission inventory from the Intergovernmental Panel for Climate Change (IPCC). In addition, significantly elevated aerosol loading has been documented over the Pacific under the influence of Asian pollution outflows on the basis of aircraft and satellite measurements[8,9,33]. For the three aerosol cases, fixed aerosol concentrations (as the initial values) are assumed on the domain boundaries, with advection of aerosols from the lateral boundaries into the model domain occurring under favourable wind conditions. The calculated aerosol optical depth is around 0.55 at the model boundaries and about 0.20 averaged over the inner domain, consistent with satellite measurements from the Moderate Resolution Imaging Spectroradiometer (MODIS) in the Gulf of Mexico region. Several processes are considered for ice nucleation, including deposition and immersion, contact, and homogeneous freezing[20,31]. The removal of aerosols includes activation to form cloud droplets and ice crystals, but precipitation scavenging is not included in the present simulations. It is estimated that less than 10% of aerosols entrained from the model boundary are transported into the eyewall region, whereas the remaining amount is washed out by activation. A fixed model boundary and domain are assumed throughout our simulations. The aerosol radiative effect in the long-wave radiation is negligible compared to that in the short-wave radiation[21].

Received 12 November 2013; accepted 27 January 2014; published online 9 March 2014

References

1. Emanuel, K. A. Increasing destructiveness of tropical cyclones over the past 30 years. *Nature* **436,** 686–688 (2005).
2. Webster, P. J., Holland, G. J., Curry, J. A. & Chang, H. R. Changes in tropical cyclone number, duration, and intensity in a warming environment. *Science* **309,** 1844–1846 (2005).
3. Holland, G. J. & Webster, P. J. Heightened tropical cyclone activity in the North Atlantic: Natural variability or climate trend?. *Phil. Trans. R. Soc. A* **365,** 2695–2716 (2007).
4. Knutson, T. R. *et al.* Tropical cyclones and climate change. *Nature Geosci.* **3,** 157–163 (2010).
5. Rosenfeld, D. *et al.* Aerosol effects on microstructure and intensity of tropical cyclones. *Bull. Amer. Meteorol. Soc.* **93,** 987–1001 (2012).
6. Emanuel, K. A. Downscaling CMIP5 climate models show increased tropical cyclone activity over the 21st century. *Proc. Natl Acad. Sci. USA* **110,** 12219–12224 (2013).
7. Dunstone, N. J., Smith, D. M., Booth, B. B., Hermanson, L. & Eade, R. Anthropogenic aerosol forcing of Atlantic tropical storms. *Nature Geosci.* **6,** 534–539 (2013).
8. Zhang, R. *et al.* Intensification of Pacific storm track linked to Asian pollution. *Proc. Natl Acad. Sci. USA* **104,** 5295–5299 (2007).
9. Li, G., Wang, Y., Lee, K-H., Diao, Y. & Zhang, R. Increased winter precipitation over the North Pacific from 1984–1994 to 1995–2005 inferred from the Global Precipitation Climatology Project. *Geophys. Res. Lett.* **35,** L13821 (2009).
10. Wang, Y., Zhang, R. & Saravanan, R. Asian pollution climatically modulates mid-latitude cyclones following hierarchical modelling and observational analysis. *Nature Commun.* **5,** 3098 (2014).
11. Fan, J., Zhang, R., Li, G. & Tao, W-K. Effects of aerosols and relative humidity on cumulus clouds. *J. Geophys. Res.* **112,** D14204 (2007).
12. Mann, M. E. & Emanuel, K. A. Atlantic hurricane trends linked to climate change. *Eos Trans.* **87,** 233–244 (2006).

13. Lau, K. M. & Kim, K.-M. How nature foiled the 2006 hurricane forecasts. *Eos Trans.* **88,** 105–107 (2007).
14. Dunion, J. P. & Velden, C. S. The impact of the Saharan air layer on Atlantic tropical cyclone activity. *Bull. Am. Meteor. Soc.* **85,** 353–365 (2004).
15. Zhang, H., McFarquhar, G. M., Saleeby, S. M. & Cotton, W. R. Impacts of Saharan dust as CCN on the evolution of an idealized tropical cyclone. *Geophys. Res. Lett.* **34,** L14812 (2007).
16. Khain, A. P., Cohen, N., Lynn, B. & Pokrovsky, A. Possible aerosol effects on lightning activity and structure of hurricanes. *J. Atmos. Sci.* **65,** 3652–3677 (2008).
17. Carrió, G. G. & Cotton, W. R. Investigations of aerosol impacts on hurricanes: Virtual seeding flights. *Atmos. Chem. Phys.* **11,** 2557–2567 (2011).
18. Zhang, H., McFarquhar, G. M., Cotton, W. R. & Deng, Y. Direct and indirect impacts of Saharan dust acting as cloud condensation nuclei on tropical cyclone eyewall development. *Geophys. Res. Lett.* **36,** L06802 (2009).
19. Rosenfeld, D., Khain, A., Lynn, B. & Woodley, W. L. Simulation of hurricane response to suppression of warm rain by sub-micron aerosols. *Atmos. Chem. Phys.* **7,** 3411–3424 (2007).
20. Li, G., Wang, Y. & Zhang, R. Implementation of a two-moment bulk microphysics scheme to the WRF model to investigate aerosol–cloud interaction. *J. Geophys. Res.* **113,** D15211 (2008).
21. Fan, J. *et al.* Effects of aerosol optical properties on deep convective clouds and radiative forcing. *J. Geophys. Res.* **113,** D08209 (2008).
22. Levy, M. *et al.* Measurements of submicron aerosols in Houston, Texas during the 2009 SHARP field campaign. *J. Geophys. Res.* **118,** 10518–10534 (2013).
23. Bates, T. S. *et al.* Boundary layer aerosol chemistry during TexAQS/GoMACCS 2006: Insights into aerosol sources and transformation processes. *J. Geophys. Res.* **113,** D00F01 (2008).
24. Zhang, F., Weng, C. Y., Sippel, J. A., Meng, Z. & Bishop, C. H. Cloud-resolving hurricane initialization and prediction through assimilation of Doppler radar observations with an ensemble Kalman filter. *Mon. Weat. Rev.* **137,** 2105–2125 (2009).
25. Komaromi, W. A., Majumdar, S. J. & Rappin, E. D. Diagnosing initial condition sensitivity of Typhoon Sinlaku and Hurricane Ike. *Mon. Weat. Rev.* **139,** 3224–3242 (2008).
26. Fan, J. *et al.* Microphysical effects determine macrophysical response for aerosol impacts on deep convective clouds. *Proc. Natl Acad. Sci. USA* **110,** E4581–E4590 (2013).
27. Hawkins, H. F. & Imbembo, S. M. The structure of a small, intense hurricane—Inez 1966. *Mon. Weat. Rev.* **104,** 418–442 (1976).
28. Khain, A. P., Lynn, B. & Dudhia, J. Aerosol effects on intensity of landfalling hurricanes as seen from simulations with WRF model with spectral bin microphysics. *J. Atmos. Sci.* **67,** 365–384 (2010).
29. Lin, N. H. *et al.* An overview of regional experiments on biomass burning aerosols and related pollutants in Southeast Asia: From BASE-ASIA and the Dongsha Experiment to 7-SEAS. *Atmos. Environ.* **78,** 1–19 (2013).
30. Lau, K. M. & Zhou, Y. P. Observed recent trends in tropical cyclone rainfall over the North Atlantic and the North Pacific. *J. Geophys. Res.* **117,** D03104 (2012).
31. Fan, J. *et al.* Simulations of cumulus clouds using a spectral microphysics cloud resolving model. *J. Geophys. Res.* **112,** D04201 (2007).
32. Wang, M. *et al.* The multi-scale aerosol-climate model PNNL-MMF: Model description and evaluation. *Geosci. Model Dev.* **4,** 137–168 (2011).
33. Zhao, C. *et al.* Aircraft measurements of cloud droplet spectral dispersion and implications for indirect aerosol radiative forcing. *Geophys. Res. Lett.* **33,** L16809 (2006).

Acknowledgements

Y.W. was supported by a NASA graduate fellowship in Earth Sciences. R.Z. acknowledges support from the Ministry of Science and Technology of China under award number 2013CB955800. We thank K.A. Emanuel, P. Liss, C. Schumacher and F. Zhang for helpful discussions. Supercomputing computational facilities were provided by the Texas A&M University. Y.W. acknowledges additional support by the NASA ROSES COUND program at the Jet Propulsion Laboratory, California Institute of Technology, under contract with NASA.

Author contributions

K.L., Y.W. and R.Z. designed the research. K.L. and Y.W. conducted the research (performed the model simulations and analysed the data). Y.W., Y.L. and M.L. performed additional ensemble simulations and analysis. Y.W. and R.Z. wrote the manuscript.

Additional information

Supplementary information is available in the online version of the paper. Reprints and permissions information is available online at www.nature.com/reprints. Correspondence and requests for materials should be addressed to Y.W. and R.Z.

Competing financial interests

The authors declare no competing financial interests.